Revisiting particle dry deposition and its role in radiative effect estimates

Ethan W. Emerson[a,b], Anna L. Hodshire[a,c], Holly M. DeBolt[a], Kelsey R. Bilsback[c], Jeffrey R. Pierce[c], Gavin R. McMeeking[b], and Delphine K. Farmer[a,1]

[a]Department of Chemistry, Colorado State University, Fort Collins, CO 80523; [b]Handix Scientific LLC, Boulder, CO 80301; and [c]Department of Atmospheric Sciences, Colorado State University, Fort Collins, CO 80523

Edited by John H. Seinfeld, California Institute of Technology, Pasadena, CA, and approved August 26, 2020 (received for review July 14, 2020)

Wet and dry deposition remove aerosols from the atmosphere, and these processes control aerosol lifetime and thus impact climate and air quality. Dry deposition is a significant source of aerosol uncertainty in global chemical transport and climate models. Dry deposition parameterizations in most global models were developed when few particle deposition measurements were available. However, new measurement techniques have enabled more size-resolved particle flux observations. We combined literature measurements with data that we collected over a grassland in Oklahoma and a pine forest in Colorado to develop a dry deposition parameterization. We find that relative to observations, previous parameterizations overestimated deposition of the accumulation and Aitken mode particles, and underestimated in the coarse mode. These systematic differences in observed and modeled accumulation mode particle deposition velocities are as large as an order of magnitude over terrestrial ecosystems. As accumulation mode particles form most of the cloud condensation nuclei (CCN) that influence the indirect radiative effect, this model-measurement discrepancy in dry deposition alters modeled CCN and radiative forcing. We present a revised observationally driven parameterization for regional and global aerosol models. Using this revised dry deposition scheme in the Goddard Earth Observing System (GEOS)-Chem chemical transport model, we find that global surface accumulation-mode number concentrations increase by 62% and enhance the global combined anthropogenic and natural aerosol indirect effect by −0.63 W m^{-2}. Our observationally constrained approach should reduce the uncertainty of particle dry deposition in global chemical transport models.

dry deposition | aerosols | radiation | eddy covariance

The lifetime of particles in the atmosphere is determined by wet and dry deposition. Wet deposition removes particles by precipitation or in-cloud processing, while dry deposition directly uptakes particles to terrestrial surfaces (1). Wet deposition losses are typically estimated to account for the majority of submicron particle removal from the atmosphere—for example, models and measurements suggest >80% of black carbon mass loss from the atmosphere is due to wet deposition (2, 3). However, dry deposition remains a globally important first-order loss process that scales with concentration and is critical for estimating accurate spatial and temporal aerosol distributions in atmospheric models (1, 4, 5).

The two largest sources of uncertainty associated with anthropogenic climate forcing are the direct and indirect aerosol effects. Aerosols scatter or absorb radiation through the direct effect, thereby cooling or warming the climate directly. Aerosols also interact with clouds to cause the indirect effect by altering cloud droplet concentration, cloud albedo, and precipitation (6). Cloud droplet concentrations, along with cloud albedo and precipitation rates, are affected by cloud condensation nuclei (CCN) concentrations (generally, the number concentration of particles with diameters larger than 50–100 nm). CCN are small particles on which cloud droplets activate (7). Dry deposition rates of particles directly impact model estimates of particle and CCN concentrations, and thus both the direct and indirect effects. Dry deposition in the accumulation mode (0.1 to 1 μm) is the single process that contributes the most uncertainty to global CCN predictions (8). Improving our understanding of dry deposition of accumulation mode particles can directly reduce uncertainties in the radiative effects of aerosols.

The treatment of dry deposition in most global models stems from theoretical work conducted by Slinn (9–11). This parameterization and its derivatives, including the widely used parameterization from Zhang et al. (12), are often implemented in air-quality models (12–15). These parameterizations generally predict a size-dependent deposition velocity with a minimum at particle diameters of ∼1 μm (for land surfaces). There were few particle flux measurements over the terrestrial biosphere at the time of Slinn's pioneering work. Since then, direct measurements of particle deposition have progressed substantially. As we will show below, these measurements suggest that the deposition velocity minimum occurs closer to ∼0.1 μm, at the lower bound of the accumulation mode and an order of magnitude smaller than previously thought. We explore the evidence for, and implications of, this revised particle dry deposition parameterization below.

Resistance Models of Dry Deposition

Dry deposition is typically described using a resistance model that includes gravitational setting (V_g) and a series of two resistors to describe the aerodynamic (R_a) and surface resistances (R_s):

Significance

Dry deposition is a key sink of atmospheric particles, which impact human and ecosystem health, and the radiative balance of the planet. However, the deposition parameterizations used in climate and air-quality models are poorly constrained by observations. Dry deposition of submicron particles is the largest uncertainty in aerosol indirect radiative forcing. Our particle flux observations indicate that dry deposition velocities are an order of magnitude lower than models suggest. Our updated, observation-driven parameterizations should reduce uncertainty in modeled dry deposition. The scheme increases modeled accumulation mode aerosol number concentrations, and enhances the combined natural and anthropogenic aerosol indirect effect by −0.63 W m^{-2}, similar in magnitude to the total aerosol indirect forcing in the Intergovernmental Panel on Climate Change report.

Author contributions: G.R.M. and D.K.F. designed research; E.W.E., A.L.H., H.M.D., K.R.B., J.R.P., G.R.M., and D.K.F. performed research; E.W.E., A.L.H., K.R.B., and J.R.P. analyzed data; and E.W.E. and D.K.F. wrote the paper.

The authors declare no competing interest.

This article is a PNAS Direct Submission.

[1]To whom correspondence may be addressed. Email: delphine.farmer@colostate.edu.

This article contains supporting information online at https://www.pnas.org/lookup/suppl/doi:10.1073/pnas.2014761117/-/DCSupplemental.

First published October 5, 2020.

$$V_d(d_p) = V_g(d_p) + \frac{1}{R_a + R_s}. \quad [1]$$

Under stable conditions, the aerodynamic resistance term dominates, but under turbulent conditions, the surface resistance term dominates (13). The surface resistance term includes the loss efficiency of particles by three processes: Brownian diffusion (E_b), impaction (E_{Im}), and interception (E_{In}). The loss of particles by Brownian motion is a result of diffusion of the particle from near the surface to the surface of a collector. Impaction is the direct collision of a particle to a surface resulting from the particle's inertia preventing it from following the streamlines around a collector surface. Interception is a similar process to impaction, but describes the instances when the particle comes within a single-particle radius of the collector and is captured. Modeled particle loss due to Brownian diffusion and impaction occurs over all land use types, but interception only occurs over surfaces that have collectors (e.g., trees, grasses, leaves) that can be described with a cross-sectional radius.

$$R_s = \frac{1}{\varepsilon_0 U_*(E_b + E_{Im} + E_{In})\, R_1}. \quad [2]$$

These terms make up the overall surface resistance in conjunction with an empirical coefficient (ε_0), friction velocity (U_*), and a bounce correction term, R_1 (12). The loss efficiency of particles by Brownian diffusion, impaction, and interception is size dependent and contains empirical coefficients that are adjusted to describe observations—although we note that these adjustments have been modified infrequently since the original 1980 studies:

$$E_B = C_b Sc^{-2/3}, \quad [3]$$

$$E_{Im} = C_{Im}\left(\frac{St}{\alpha + St}\right)^{\beta}, \quad [4]$$

$$E_{In} = C_{In}\left(\frac{d_p}{A}\right)^{\nu}. \quad [5]$$

These equations depend on the land use dependent constant (A), particle diameter dependent parameters (Stokes number: St and the Schmidt number: Sc), and all others are empirical coefficients that were developed to describe the observations at the time. Of these three equations, only the interception efficiency (Eq. **5**) depends on surface properties (i.e., land use type) to which particles deposit.

A Revised Parameterization

We collected extensive measurements of size-resolved particle fluxes over both a pine forest and grassland (*Methods*). Similar to other recent studies (e.g., 16, 17), we find strong observational evidence that the minimum dry deposition velocity occurs at a diameter over an order of magnitude smaller compared to previous descriptions (<0.1 versus >1 μm). Fig. 1 summarizes size-resolved particle deposition velocities from our observations over a grassland and forest, other literature observations, the commonly used Zhang parameterization (18), and our revised parameterization (described below). The Zhang parameterization fails to represent recent observational evidence, including our own observations. Newer parameterizations (18–22) are more consistent with these observations, but GEOS-Chem and other chemical transport models still typically implement Zhang et al.'s parameterization (12). The newer parameterizations vary from completely empirical (21) to incorporating additional, unknown loss processes (22)—but are rarely incorporated into global models, likely due to the complexity of updated parameterizations.

Three particle loss mechanisms—gravitational settling and the Brownian and impaction collection efficiencies—drive the location of the minimum in the Zhang parameterization (Fig. 2*A*). We emphasize that the minimum of the Zhang parameterization is consistent with flux measurements available at the time. However, these measurements were taken over smooth and nonvegetated surfaces, and critically, particle deposition was less influenced by the interception loss mechanism. Considering the wealth of measurements now available over evergreen needle leaf forests, it is evident that interception is a key component of particle dry deposition that was underemphasized in the original parameterizations, as we will describe below. In a sophisticated model of particle dry deposition, Petroff and Zhang (23) demonstrated that changing interception can shift the minimum deposition velocity toward smaller particles. While Petroff and Zhang's model captured observations better than most previous approaches, it relied on changes to the functional form of the parameterizations, including increased numbers of land use categories, making it challenging to simply adapt to existing deposition modules in chemical transport models. Instead, a simple parameterization that relies on empirical changes to the existing and commonly used Zhang parameterization would be far simpler to employ in models. However, such a modification requires a fundamental understanding of the role of turbulence strength (described by friction velocity, U_*) in controlling particle deposition velocity.

Our extensive particle flux measurements over a pine forest enabled us to investigate turbulence effects on deposition, and thus constrain the empirical coefficients of the original Zhang approach (based on the Slinn framework) into a revised parameterization that fits both our and previously published data in both size dependence and deposition velocity magnitude (Fig. 1 and *SI Appendix*, Fig. S1). Over the accumulation mode, our observations from the Seasonal Particles in Forest Flux studY (SPiFFY) suggest that the Zhang parameterization 1) overestimates deposition velocity as a function of U_* for small particles (<100 nm), 2) captures deposition velocities well at the center of the accumulation mode (150–285 nm), and 3) underestimates (by a factor of 2 or more) deposition velocity for larger particles (>400 nm). Poor counting statistics limit our observations for larger particles (>400 nm), but previous studies fill in the gaps.

In concert with relatively small changes to the Brownian diffusion coefficients, our revised parameterization incorporates a larger role for interception based on our observations showing consistent underestimation of fluxes over more vegetated surfaces—and the observed differences between the forest and grassland sites (Fig. 2*B*). Our revised parameterization shifts the minimum deposition velocity to smaller particles, consistent with our and other observations over needle leaf forests. *SI Appendix*, Table S1 presents the revised parameterization. Specifically, we modified six empirical coefficients, all independent of land use, based on a substantial number of measurements that were not previously available. Our parameterization is simple enough to be easily included in chemical transport models on multiple scales. To this end, we investigated how this updated parameterization impacts aerosol concentrations, radiative effects, and CCN in a global chemical transport model.

Our modified parameterization can describe observations across a variety of land use types: deciduous forest, coniferous forest, agricultural land, and water (Fig. 1). Over these four land use types, our parameterization captures most observations within an order of magnitude uncertainty, implying a far smaller degree of uncertainty in dry deposition parametrizations than previously possible. For example, Lee et al. (8) suggested that the uncertainty in dry deposition velocity was two orders of magnitude in their assessment of uncertainties contributing to the CCN indirect effect—of which dry deposition was identified as the dominant source of uncertainty. We note that while some of the measurements appear outside of the order of magnitude bounding region

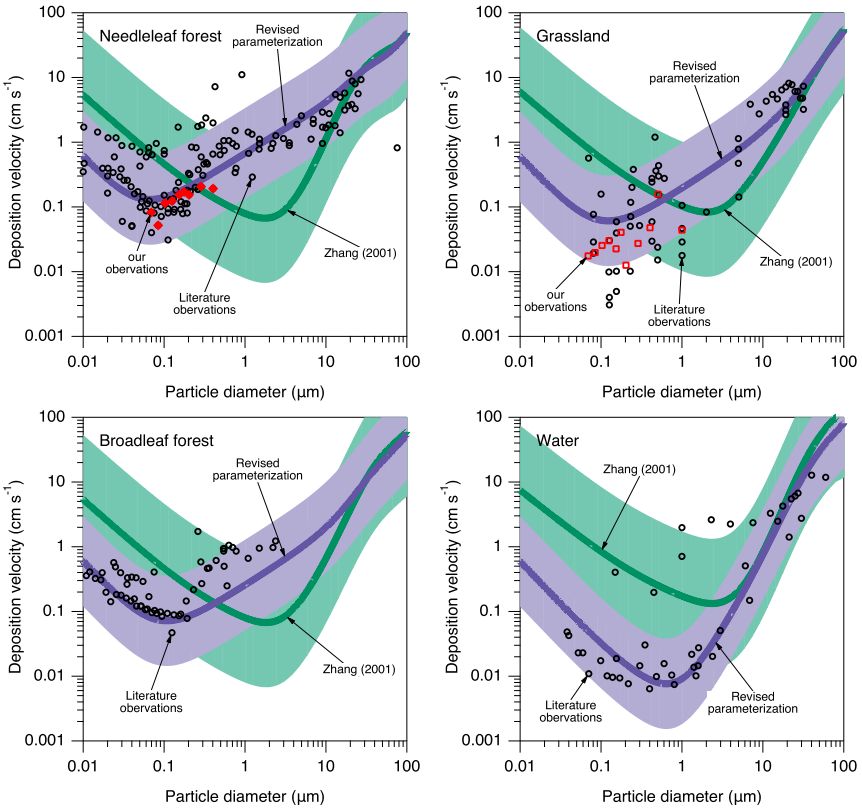

Fig. 1. Dry deposition velocities as a function of particle diameter across four land use types used in GEOS-Chem. Literature observations are shown, as is the Zhang parameterization (current default in GEOS-Chem, green) and our revised parameterization (purple). Both parameterizations assume particle density is 1,200 kg m^{-3}, particle water uptake corresponding to ambient relative humidity, and U_* of 0.2 m s^{-1}, although the observations may vary from this value. The bounding range for the Zhang parameterization spans two orders of magnitude, while we propose a 5× bounding range. Observations are shown in red for the needle leaf and grassland land use types.

in Fig. 1, the model line uses a single assumed U_* that may not be representative of that particular measurement. The parameterization can be used for a sensible or measured value of U_*. For example, our SPiFFY observations over a coniferous forest are consistent with a 5× bounding region that describes 95% of the variability of measured deposition velocities when the observed U_* values are accounted for. There are fewer particle flux observations over the remaining land use types, particularly for particles <100 nm over grasslands. However, available data suggest that deposition velocities over both terrestrial and water surfaces show a similar submicron diameter minimum to coniferous forest, which is far better captured by our revised parameterization than the previous Zhang approach. The parameterization over water surfaces is distinct from terrestrial surfaces because there can be no interception over a flat surface and thus the size dependence is driven only by Brownian diffusion and impaction, resulting in a stronger U_* dependence in the accumulation mode. As water is the dominant surface over earth, this revision in dry deposition may have substantial consequences for the global atmospheric lifetime of particles—although it is possible that under strong wind conditions,

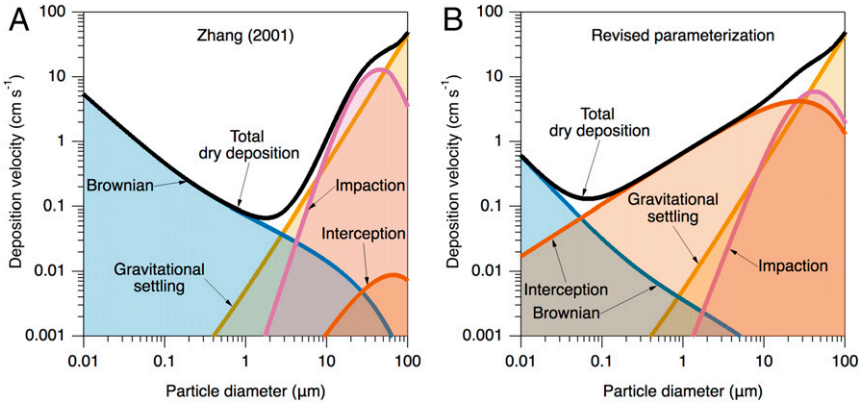

Fig. 2. Contributions from the three collection efficiencies governing the surface resistance and gravitational settling are contrasted for the Zhang et al. (12) parameterization (*A*) and our revised parameterization (*B*) for evergreen needle leaf forests. Our revised parameterization increases the role of interception following recently available observational evidence. Models consider U_* = 0.4 m s^{-1}, and assumed a particle density of 1,500 kg m^{-3}.

waves provide enough surface structure to enable interception. Additional particle flux measurements over the diversity of land use types, including water, cryosphere, and urban systems, would be useful tests of this new parameterization.

Overall, the observational data support a narrower uncertainty bound for this revised dry deposition parameterization over terrestrial and water surfaces, although additional observations are essential for further validating our approach.

Impact on Modeled Number Concentrations, CCN, and Radiative Effects

Our revised dry deposition treatment has substantial impacts on global aerosols, altering their lifetime and thus ambient concentrations at the surface (Fig. 3). Using a global chemical transport model with detailed aerosol microphysics (GEOS-Chem-TOMAS) (TwO-Moment Aerosol Sectional) that predicts size-resolved particle concentrations between 3 nm and 10 μm, we find that these changes impact the modeled first aerosol indirect effect (i.e., cloud-albedo), direct effect, and aerosol number and mass concentrations (Figs. 3 and 4). Importantly, the direction and magnitude of these changes in modeled aerosol concentrations are size-dependent. Generally, deposition velocities of particles in the Aitken mode and much of the accumulation mode decrease relative to the Zhang parameterization, which leads to longer aerosol lifetimes and increased particle concentrations, on average. Fig. 3 shows the percent changes in aerosol number concentrations at the surface from updating the Zhang parameterization to the revised scheme. In the accumulation mode, the number concentration of particles with diameters between 100 and 500 nm (N100-500; Fig. 3*B*) show the strongest increase with the revised parameterization (62% globally averaged, 38% averaged over land, 80% averaged over oceans), due to their order-of-magnitude decrease in dry deposition velocities in the revised parameterization. Between 500 nm and 2 μm (N500-2000; Fig. 3*C*), the new parameterization crosses the original scheme to have faster deposition rates over most land surface types. Subsequently, particles between 2 and 10 μm (N2000-10000) have decreasing concentrations over nearly all land areas. N500-2000 increases by an average of 23% over oceans and an average of 2% over land due to variability between land types. N2000-10000 instead increases by only 6% over oceans but decreases by 21% over land. Overall, N500-2000 and N2000-10000 show modest changes globally (17 and −0.5%, respectively). The Aitken-mode changes between 3–100 nm (N3-100; Fig. 3*A*) are more complicated. The new parameterization slows dry deposition in this region leading to increased concentrations; however, there are regions of decreased concentrations due to microphysical feedbacks (the increases in N100-500 cause reductions in nucleation and growth rates and increases in coagulational loss rates of the small particles). Overall, N3-100 increases by 47% globally, 67% over oceans, and −1% over land.

In Fig. 4, we show the broader impacts of the dry deposition changes. Cloud-droplet number concentrations (CDNC) at low-cloud level (~900 hPa) increase by 10–30% over most of the globe (Fig. 4*C*), driven by increases in accumulation mode particles (Fig. 3*B*). The cloud-albedo aerosol indirect effect (Fig. 4*A*) from these CDNC changes (including changes to both anthropogenic and natural aerosols) is −0.63 W m^{-2} averaged globally. The effect is strongest over oceans. Over land surfaces, the decrease is smaller, but still substantial (−0.13 W m^{-2}). For context, the likely range for estimated radiative forcing from aerosol–radiation and aerosol–cloud interactions is −0.4 to −1.5 W m^{-2} (24)—although we emphasize that the number in our study is a difference between two present-day simulations with different dry deposition schemes. Ocean surfaces are a major driver of modeled changes to the aerosol indirect effect for our updated versus Zhang parameterization (e.g., Southern Ocean) as dry deposition velocities in the revised parameterization over that surface type are reduced by an order of magnitude for CCN-relevant particle sizes.

The changes in particle concentrations due to updating from the Zhang scheme to our revised scheme increases the aerosol direct effect cooling tendency by −0.09 W m^{-2} globally (including both anthropogenic and natural aerosols). However, this globally averaged negative effect is driven by predicted changes in particle concentrations over the oceans with the new

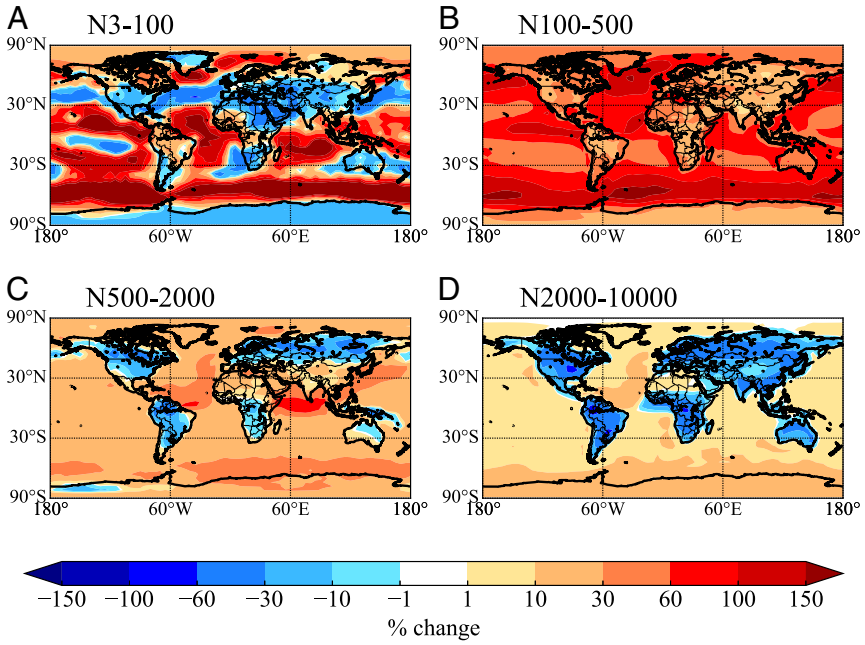

Fig. 3. Percent change of aerosol number concentration for various size ranges at the surface for GEOS-Chem-TOMAS simulations using the revised dry deposition parameterization relative to simulations with the default parameterization. Warm red colors indicate more particles when using our revised dry deposition scheme; cool blue colors are the opposite. (*A*–*D*) NX-Y refers to the number concentrations of particles within a size range (e.g., N3-100 is the number concentration of particles with diameters between 3 and 100 nm).

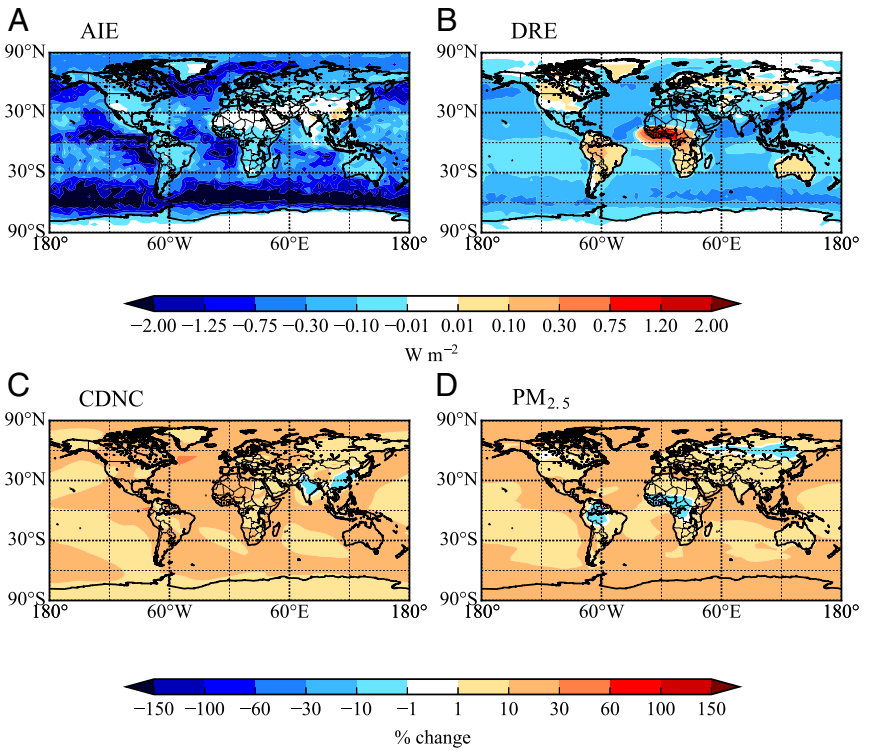

Fig. 4. The change between GEOS-Chem-TOMAS simulations using the revised parameterization relative to the simulations with the default parameterization for: (*A*) cloud-albedo aerosol indirect effect, (*B*) aerosol direct effect (externally mixed), (*C*) CDNC at 900 hPa, and (*D*) $PM_{2.5}$ mass concentration at the surface. The aerosol radiative effects (*A* and *B*) are the total change across both anthropogenic and natural aerosols in W m^{-2}. The changes in CDNC and $PM_{2.5}$ are in percent difference.

deposition parameterizations. In contrast, land surfaces show a slight positive effect (change of +0.02 W m^{-2}), which is most pronounced over sub-Saharan Africa, South America, Australia, Greenland, and scattered parts of North America and Eurasia. Thus overall, relative to the base case (default dry deposition parameterization in GEOS-Chem), the revised parameterization decreases both the aerosol indirect and direct effects.

In addition to implications for estimating radiative effects on climate, the improved treatment of dry deposition through our revised parameterization has implications for modeling air pollution and impacts on human health. For example, exposure to $PM_{2.5}$ (total mass of particles <2.5 μm in diameter) is linked to respiratory and cardiovascular disease (25). Our revised parameterization increases surface $PM_{2.5}$ concentrations by 11% globally and by 6.5% over land relative to the Zhang parameterization. Changes in $PM_{2.5}$ concentrations are observed globally and not limited to a single land use type (Fig. 4*D*). By changing the deposition velocities over the health relevant size ranges, we predict $PM_{2.5}$ to increase by 6.5% over terrestrial areas.

Implications

Our observations and previous work clearly show that dry deposition is not accurately described by the schemes used in most atmospheric models. However, our observationally constrained revision of the dry deposition parameterization has substantial impacts on predicted aerosol concentrations and their radiative and potentially health impacts. The updated models must be holistically tested against suites of observational data, particularly in remote regions, and potentially other model schemes with uncertainties (such as emissions, chemistry, or wet deposition) may need to be adjusted to compensate for the dry deposition updates.

Relative to the expert elicitation in Lee et al. (8), our work decreases the uncertainty bounds around size-resolved particle dry deposition. However, our knowledge of particle deposition remains incomplete. Gaining process-level insight into dry deposition across the size distribution will help to further reduce deposition-related uncertainty in global climate models. More eddy covariance flux measurements across a variety of land use types, particularly water surfaces, are essential, as is an improved understanding of the spatial variability of subgrid processes within individual model grid boxes through additional modeling and measurement. Improving our description of particle deposition requires a better understanding of how rapid changes in relative humidity controls particle diameter on the timescales of turbulent eddies. Further, our understanding of deposition over water surfaces requires an improved understanding of the extent to which flat versus undulating surfaces (e.g., oceans) could change the impaction term. Finally, we note that many eddy covariance data are collected in remote sites with uniform terrain, but understanding the processes that control particle dry deposition under more heterogeneous surfaces and turbulence conditions is essential for validating model parameterizations.

Conclusion

Particle dry deposition is challenging to observe, but recent advances in aerosol instrumentation have enabled numerous dry deposition measurements over a variety of land use types in the last 20 y, including our two new datasets. Collectively, these measurements clearly demonstrate that existing dry deposition parameterizations in aerosol models poorly represent observations. We suggest a revised parameterization that follows the Zhang and Slinn frameworks. Importantly, we suggest that the lack of data over coniferous forests and other complex surfaces hindered the previous approaches from accurately capturing the importance of interception as a component of dry deposition. Increasing the collection efficiency by interception over land use

surfaces, coupled to modifications in Brownian diffusion, shifts the deposition velocity minimum from particles with a diameter of 2 to 0.1 μm. Our revised parameterization fits our and literature observations in terms of both size dependence and magnitude, is extremely simple to implement in existing chemical transport models, and accurately considers the role of turbulence on deposition.

Dry deposition may be typically overlooked in global climate models, but our study points to its importance in accurately predicting radiative balance on global and regional scales. The implications of revisiting particle dry deposition on aerosol concentrations and direct and indirect effects suggest that aerosol sources and measurements must be similarly revisited.

Methods

Observations. This study uses data from two field campaigns: 1) the five distinct measurement periods of the SPiFFY study at the Manitou Experimental Forest and 2) the Black Carbon Aerosol Deposition Study (BCADS 2017) campaign at the southern Great Plains (2). Both sites were described previously (26–30).

Instruments were housed in a temperature-controlled enclosure at the base of the measurement tower during both field campaigns. During SPiFFY, the inlet was located 26 m above ground level with an inlet length of ∼30 m (3/8-in. inner diameter copper tubing) with a turbulent flow rate of 19 L min^{-1} and a residence time of 3 s. During BCADS, the inlet was located 2.7 m above ground level with a length of ∼4.5 m of 4.3-mm internal diameter stainless-steel tubing operated at 12 L min^{-1} and a residence time of 0.3 s. In both field campaigns the inlet was aligned downward (45° ± 15° angle), with a wire mesh screen to exclude insects and large debris contamination, and proximal to the sonic anemometer (slightly below in both cases, <50 cm distance).

Particles at ambient relative humidity were detected by sampling off the bypass line at 0.6 cm^3 s^{-1} using the Ultra-High Sensitivity Aerosol Spectrometer (UHSAS, Droplet Measurement Technologies, Inc.) operating with a 1,054-nm wavelength laser counting particles with an optical diameter from 60 nm to 100 nm at 10 Hz. Particles were collected into 99 original-size bins that were aggregated into 12 bins (diameter ranges in nanometers): 60–70, 70–84, 84–103, 103–126, 126–153, 153–177, 177–204, 204–286, 286–403, 403–506, 506–711, and 711–1,000. The UHSAS operated on its own internal computer collecting data at 10 Hz with continuous timestamps. The UHSAS was calibrated prior to each field campaign with polystyrene latex spheres.

At SPiFFY, three-dimensional high-frequency (10-Hz) windspeed data were collected using a Campbell CSAT III anemometer during summer 2015, winter 2016, spring 2016, and summer 2016 and an Applied Technologies Inc. A-probe sonic anemometer during fall 2016. These data were collected on a separate computer, and timestamps were synced. During BCADS, windspeed was collected using the Gill Instruments WindMaster Pro and were corrected per technical note KN1509v3 (31).

We measure surface-atmosphere exchange with the eddy covariance flux technique. This technique measures the vertical flux (F_c) for a given scalar crossing the measurement plane of a horizontally homogeneous area. F_c is determined by the covariance of the vertical windspeed (w) and scalar (*c;* e.g., particle concentration)

$$F_c = \overline{w'c'} = \frac{1}{n}\sum_{i=0}^{n}(c_i - \bar{c})\,(w_i - \overline{w}), \quad [6]$$

where n is the number of points used in the calculation, w_i and c_i are instantaneous measurements of vertical windspeed and scalar, respectively, and $\overline{w}$ and $\bar{c}$ are the mean values. (32) Eddy covariance flux measurements can be calculated over varying timescales, but 30 min is typical and employed here. The deposition velocity is determined from the flux and the mean concentration over the 30-min flux period as

$$F_c = -V_d\bar{c}, \quad [7]$$

where a positive V_d indicates deposition and a negative V_d implies an emission process.

We calculated eddy covariance fluxes of size-resolved particle bins:

1) Particle diameter was calculated from the UHSAS data.
2) Timelag correction: Scalar data were corrected for the timelag between the sonic and UHSAS data using bypass flow rates (−3 and −0.3 s for the SPiFFY and BCADS campaigns, respectively).
3) Sonic rotation: A two-dimensional rotation of windspeed in three axes accounted for the sonic anemometer not being precisely level with the ground. (33, 34).
4) Eq. **18** calculates eddy covariance fluxes.
5) Quality controls:
   - The stationarity test ensures that calculated fluxes do not vary substantially within the timescale of analysis (35).
   - We remove flux periods with an average wind direction that was obstructed by the sampling tower.
6) Storage correction: During horizontally homogeneous conditions, the turbulent flux below the measurement height can be different. Due to a lack of below-sensor measurements, we use a one-point storage term developed by Rannik et al. (36):

$$F_{storage} = \int_0^{z_r}\frac{\partial\overline{c}}{\partial t}dz \approx z_r\frac{\overline{c(t+\Delta T)} - \overline{c(t)}}{\Delta T} \quad [8]$$

   where c is the concentration and $t = 2$ min with $\Delta T = 30$ min. These values were calculated for all flux periods that ended within 10 s of the next one starting. We considered other data corrections (storage, time response, sensor separation, tube attenuation, Webb–Pearman–Leuning, despiking, and detrending), but did not include them as they were either inappropriate or resulted in negligible changes to the calculated fluxes.
7) Uncertainty: We determined an average limit of detection (LOD) (37):

$$\overline{\mathrm{LOD}} = \frac{1}{N}\sqrt{\sum_{i=1}^{N}(\alpha \times RE_i)^2}, \quad [9]$$

   where α is a specified confidence interval ($\alpha = 3$ for the 99th percentile) and RE_i is the error of a particular flux period as calculated using Finkelstein and Sims (ref. 38). We propagate the flux limit of detection to a deposition velocity limit of detection.
8) Spectral analysis: Eddy covariance requires a sufficiently fast sensor response time. The UHSAS as well as other particle-counting methods meet this criterion (16, 17, 39). *SI Appendix*, Fig. S2 shows an example cospectrum for a day during the Summer 2015 SPIFFY campaign. The characteristic inertial subrange ($f^{-7/3}$) predicted by Kolmogorov theory (40) is observed between 0.1 and 3 Hz and demonstrates a sufficiently fast sensor response time for this instrument. Additionally, the particle data follow the sensible heat cospectrum, demonstrating a near-ideal measurement.

Modeling. All modeling used the GEOS-Chem model v12.0.3 (geos-chem.org/) coupled to the TwO-Moment Aerosol Sectional (TOMAS) microphysics model (41) to run two simulations, one with the Zhang et al. parameterization and one with our revised parameterization. This version of GEOS-Chem had 47 vertical layers, a horizontal resolution of 4° × 5°, and used GEOS-FP reanalysis meteorology. TOMAS had 15 size bins with dry diameters spanning 3 nm–10 μm. This microphysics scheme includes nucleation, condensation, coagulation, size-resolved emissions, and wet and dry deposition. TOMAS includes size-resolved organic aerosol, black carbon, sulfate, sea salt, and mineral dust species. The simulations were run for 12 mo of the model year 2016, with 1 mo of model spin up. The base anthropogenic inventory was EDGARv4.3 (42). Anthropogenic regional emissions inventories included: MIX (Asia), Diffuse and Inefficient Combustion Emissions (DICE, Africa), National Emissions Inventory (NEI2011, United States; https://www.epa.gov/air-emissions-inventories), Air Pollutant Emission Inventory (APEI, Canada; https://www.canada.ca/en/environment-climate-change/services/pollutants/air-emissions-inventory-overview.html), the Big Bend Regional Aerosol and Visibility Observational Study Emissions Inventory (BRAVO, Mexico), and the European Monitoring and Evaluation Program (EMEP, Europe; https://www.ceip.at/) (43–45). Biomass burning emissions were from the Global Fire Emissions Database, 4th Generation (46). Sea-salt emissions followed Jaeglé et al.'s scheme (47), natural dust emissions followed the Dust Entrainment and Deposition scheme (48), and secondary organic aerosols followed Pai et al. (49). For the aerosol direct radiative effect and cloud-albedo indirect effects, we used the offline Rapid Radiative Transfer Model for Global and Regional Modeling Applications (50, 51). Meteorological (form GOES-FP) and aerosol inputs (from GEOS-Chem-TOMAS) were monthly averaged for these calculations. For the aerosol direct effect, we assumed that within each TOMAS size bin black carbon was a separate particle from all other aerosol components

(i.e., "externally" mixed). For the cloud-albedo indirect effect, we used the cloud-droplet-radius perturbation method originally described in Rap et al. (52).

Data Availability. The .csv data have been deposited in Open Science Framework (53).

ACKNOWLEDGMENTS. This study was supported by the National Oceanic and Atmospheric Administration Climate Program Office's Atmospheric Chemistry, Carbon Cycle, and Climate program (Grants NA14OAR4310141 and NA17OAR4310001) and the Department of Energy Office of Biological and Environmental Research (Grants DE-SC0016259 and DE-SC0019000).

1. D. B. Schwede, G. G. Lear, A novel hybrid approach for estimating total deposition in the United States. *Atmos. Environ.* **92**, 207–220 (2014).
2. E.W. Emerson, J. M. Katich, J. P. Schwarz, G. R. McMeeking, Farmer DK direct measurements of dry and wet deposition of black carbon over a grassland. *J. Geophys. Res. Atmos.* **123**, 12,277-21,290 (2018).
3. D. Koch *et al*., Evaluation of black carbon estimations in global aerosol models. *Atmos. Chem. Phys.* **9**, 9001–9026 (2009).
4. W. Gong *et al*., Modelling aerosol-cloud-meteorology interaction: A case study with a fully coupled air quality model (GEM-MACH). *Atmos. Environ.* **115**, 695–715 (2015).
5. P. Lee *et al*., NAQFC developmental forecast guidance for fine particulate matter (PM2.5). *Weather Forecast.* **32**, 343–360 (2017).
6. U. Lohmann, J. Feichter, Global indirect aerosol effects: A review. *Atmos. Chem. Phys.* **5**, 715–737 (2005).
7. D. K. Farmer, C. D. Cappa, S. M. Kreidenweis, Atmospheric processes and their controlling influence on cloud condensation nuclei activity. *Chem. Rev.* **115**, 4199–4217 (2015).
8. L. A. Lee *et al*., The magnitude and causes of uncertainty in global model simulations of cloud condensation nuclei. *Atmos. Chem. Phys.* **13**, 8879–8914 (2013).
9. W. G. N. Slinn, Some approximations for wet and dry removal of particles and gases from atmosphere. *Water Air Soil Pollut.* **7**, 513–543 (1977).
10. S. A. Slinn, W. G. N. Slinn, Predictions for particle deposition on natural-waters. *Atmos. Environ.* **14**, 1013–1016 (1980).
11. W. G. N. Slinn, Predictions for particle deposition to vegetative canopies. *Atmos. Environ.* **16**, 1785–1794 (1982).
12. L. M. Zhang, S. L. Gong, J. Padro, L. Barrie, A size-segregated particle dry deposition scheme for an atmospheric aerosol module. *Atmos. Environ.* **35**, 549–560 (2001).
13. E. Solazzo *et al*., Operational model evaluation for particulate matter in Europe and North America in the context of AQMEII. *Atmos. Environ.* **53**, 75–92 (2012).
14. M. L. Wesely, Parameterization of surface resistances to gaseous dry deposition in regional-scale numerical models. *Atmos. Environ.* **23**, 1293–1304 (1989).
15. J. H. Seinfeld, S. N. Pandis, *Atmospheric Chemistry and Physics: From Air Pollution to Climate Change*, (John Wiley, Hoboken, NJ, ed. 2, 2006).
16. I. Mammarella *et al*., Long-term aerosol particle flux observations. Part II: Particle size statistics and deposition velocities. *Atmos. Environ.* **45**, 3794–3805 (2011).
17. M. J. Deventer, A. Held, T. S. El-Madany, O. Klemm, Size-resolved eddy covariance fluxes of nucleation to accumulation mode aerosol particles over a coniferous forest. *Agric. For. Meteorol.* **214-215**, 328–340 (2015).
18. J. Zhang, Y. Shao, A new parameterization of particle dry deposition over rough surfaces. *Atmos. Chem. Phys.* **14**, 12429–12440 (2014).
19. A. Petroff, A. Mailliat, M. Amielh, F. Anselmet, Aerosol dry deposition on vegetative canopies. Part I: Review of present knowledge. *Atmos. Environ.* **42**, 3625–3653 (2008).
20. R. Kouznetsov, M. Sofiev, A methodology for evaluation of vertical dispersion and dry deposition of atmospheric aerosols. *J. Geophys. Res. Atmos.* **117**, D01202 (2012).
21. L. Zhang, Z. He, Technical Note: An empirical algorithm estimating dry deposition velocity of fine, coarse and giant particles. *Atmos. Chem. Phys.* **14**, 3729–3737 (2014).
22. R. D. Saylor *et al*., The particle dry deposition component of total deposition from air quality models: Right, wrong or uncertain? *Tellus B Chem. Phys. Meterol.* **71**, 1550324 (2019).
23. A. Petroff, L. Zhang, Development and validation of a size-resolved particle dry deposition scheme for application in aerosol transport models. *Geosci. Model Dev.* **3**, 753–769 (2010).
24. T. F. Stocker *et al*., *Climate Change 2013: The Physical Science Basis. Contribution of Working Group I to the Fifth Assessment Report of IPCC the Intergovernmental Panel on Climate Change*, (Cambridge University Press, 2014).
25. A. J. Cohen *et al*., The global burden of disease due to outdoor air pollution. *J. Toxicol. Environ. Health A* **68**, 1301–1307 (2005).
26. M. L. Fischer, D. P. Billesbach, J. A. Berry, W. J. Riley, M. S. Torn, Spatiotemporal variations in growing season exchanges of CO2, H2O, and sensible heat in agricultural fields of the southern Great Plains. *Earth Interact.* **11**, 1–21 (2007).
27. W. J. Riley *et al*., Regional CO2 and latent heat surface fluxes in the Southern Great Plains: Measurements, modeling, and scaling. *J. Geophys. Res.* **114**, G04009 (2009).
28. D. L. Sisterson, R. A. Peppler, T. S. Cress, P. J. Lamb, D. D. Turner, The ARM southern Great Plains (SGP) site. *Meteor. Mon.* **57**, 6.1-6.14 (2016).
29. S. R. Fulgham *et al*., Seasonal flux measurements over a Colorado pine forest demonstrate a persistent source of organic acids. *ACS Earth Space Chem.* **9**, 2017–2032 (2019).
30. J. Ortega *et al*., Overview of the Manitou experimental forest observatory: Site description and selected science results from 2008 to 2013. *Atmos. Chem. Phys.* **14**, 6345–6367 (2014).
31. Gill Instruments, Software bug affecting 'w' wind component of the WindMaster family (Tech. Rep. KN1509v3, Gill Instruments, Hampshire, UK, 2016).
32. D. D. Baldocchi, B. B. Hincks, T. P. Meyers, Measuring biosphere-atmosphere exchanges of biologically related gases with micrometeorological methods. *Ecology* **69**, 1331–1340 (1988).
33. W. J. Massman, A simple method for estimating frequency response corrections for eddy covariance systems. *Agric. For. Meteorol.* **104**, 185–198 (2000).
34. J. M. Wilczak, S. P. Oncley, S. A. Stage, Sonic anemometer tilt correction algorithms. *Boundary-Layer Meteorol.* **99**, 127–150 (2001).
35. T. Foken, B. Wichura, Tools for quality assessment of surface-based flux measurements. *Agric. For. Meteorol.* **78**, 83–105 (1996).
36. Ü. Rannik *et al*., Long-term aerosol particle flux observations part I: Uncertainties and time-average statistics. *Atmos. Environ.* **43**, 3431–3439 (2009).
37. B. Langford, W. Acton, C. Ammann, A. Valach, E. Nemitz, Eddy-covariance data with low signal-to-noise ratio: Time-lag determination, uncertainties and limit of detection. *Atmos. Meas. Tech.* **8**, 4197–4213 (2015).
38. P. L. Finkelstein, P. F. Sims, Sampling error in eddy correlation flux measurements. *J. Geophys. Res. Atmos.* **106**, 3503–3509 (2001).
39. A. Petroff, J. G. Murphy, S. C. Thomas, J. A. Geddes, Size-resolved aerosol fluxes above a temperate broadleaf forest. *Atmos. Environ.* **190**, 359–375 (2018).
40. J. C. Kaimal, J. J. Finnigan, *Atmospheric Boundary Layer Flows: Their Structure and Measurement*, (Oxford University Press, 1994).
41. P. J. Adams, J. H. Seinfeld, Predicting global aerosol size distributions in general circulation models. *J. Geophys. Res. Atmos.* **107**, AAC 4-1-AAC 4-23 (2002).
42. M. Crippa *et al*., Forty years of improvements in European air quality: Regional policy-industry interactions with global impacts. *Atmos. Chem. Phys.* **16**, 3825–3841 (2016).
43. M. Li *et al*., MIX: A mosaic Asian anthropogenic emission inventory under the international collaboration framework of the MICS-Asia and HTAP. *Atmos. Chem. Phys.* **17**, 935–963 (2017).
44. E. A. Marais, C. Wiedinmyer, Air quality impact of diffuse and inefficient combustion emissions in Africa (DICE-Africa). *Environ. Sci. Technol.* **50**, 10739–10745 (2016).
45. H. Kuhns, E. M. Knipping, J. M. Vukovich, Development of a United States-Mexico emissions inventory for the big bend regional aerosol and visibility observational (BRAVO) study. *J. Air Waste Manag. Assoc.* **55**, 677–692 (2005).
46. J. T. Randerson, G. R. Van Der Werf, L. Giglio, G. J. Collatz, P. S. Kasibhatla, *Global Fire Emissions Database, Version 4.1 (GFEDv4)*, (ORNL Distributed Active Archive Center, 2017).
47. L. Jaeglé, P. K. Quinn, T. S. Bates, B. Alexander, J. T. Lin, Global distribution of sea salt aerosols: New constraints from in situ and remote sensing observations. *Atmos. Chem. Phys.* **11**, 3137–3157 (2011).
48. C. S. Zender, H. Bian, D. Newman, Mineral dust entrainment and deposition (DEAD) model: Description and 1990s dust climatology. *J. Geophys. Res. D Atmospheres* **108**, 4416 (2003).
49. S. J. Pai *et al*., An evaluation of global organic aerosol schemes using airborne observations. *Atmos. Chem. Phys.* **20**, 2637–2665 (2020).
50. J. K. Kodros, R. Cucinotta, D. A. Ridley, C. Wiedinmyer, J. R. Pierce, The aerosol radiative effects of uncontrolled combustion of domestic waste. *Atmos. Chem. Phys.* **16**, 6771–6784 (2016).
51. J. K. Kodros, J. R. Pierce, Important global and regional differences in aerosol cloud-albedo effect estimates between simulations with and without prognostic aerosol microphysics. *J. Geophys. Res. D Atmospheres* **122**, 4003–4018 (2017).
52. A. Rap *et al*., Natural aerosol direct and indirect radiative effects. *Geophys. Res. Lett.* **40**, 3297–3301 (2013).
53. D. K. Farmer, E. W. Emerson, Farmer Group Particle Flux Data. Open Science Framework. https://osf.io/htndj/. Deposited 21 September 2020.